The Meteoritical Society

Meteoritics & Planetary Science 44, Nr 1, 141–154 (2009)
Abstract available online at http://meteoritics.org

Application of a textural geospeedometer to the late-stage magmatic history of MIL 03346

Julia E. HAMMER

Department of Geology and Geophysics, University of Hawai'i 1680 East-West Rd., Honolulu, Hawai'i 96822, USA
Corresponding author. E-mail: jhammer@soest.hawaii.edu

(Received 09 April 2008; revision accepted 28 July 2008)

Abstract—Dynamic crystallization experiments performed on Fe-rich, Al-poor basalt are employed as a textural calibration set to quantify the late-stage igneous history of nakhlite Miller Range (MIL) 03346. The ratio of crystal-melt surface area to volume typifying morphologically distinct populations of Ca-pyroxene has been shown to vary as a strong function of cooling rate (Hammer 2006). Furthermore, a texture of phenocrysts surrounded by finer-grained groundmass crystals arises by sequential nucleation events during constant-rate cooling, but multiple populations nucleate only if the cooling rate is ≤72 °C h^{-1}. Textural analysis of meteorite MIL 03346 reveals at least two distinct populations. The Ca-pyroxene phenocryst and microphenocryst three dimensional (3D) aspect ratios are 112 ± 8.3 and 1530 ± 160 mm^{-1}, respectively. By comparison with the calibration set, the range of cooling rates consistent with 3D aspect ratios of both populations in MIL 03346 is ~20 °C h^{-1}. An additional experiment was performed approximating a conductive heat transfer profile in order to interpret and apply results of constant-rate cooling experiments to the natural cooling of magma. Results suggest that the textures of constant-rate experiments parallel the initial period of rapid cooling in natural magma. Initial cooling rates of ~20 °C h^{-1} in the lava hosting MIL 03346 occur in conductively solidifying lava at depths of ~0.4 m, constraining the minimum total thickness to ≥0.8 m. Crystal accumulation beginning in a subsurface reservoir and continuing after lava emplacement as an inflated pahoehoe sheet satisfies all textural constraints on the late-stage igneous history of MIL 03346.

INTRODUCTION

The nakhlite group of meteorites are clinopyroxenites with a vitrophyric groundmass and evidence of weak aqueous alteration (Treiman 2005). The most recently discovered nakhlite, Miller Range (MIL) 03346, is a 715 g specimen recovered in Antarctica's Miller Range in 2003 (McBride et al. 2005). MIL 03346 bears strong resemblance to other nakhlites as an olivine-bearing, sub-calcic augite cumulate (Day et al. 2006). However, several characteristics render it not only unique among the nakhlites, but suggest that it is the end member of a spectrum in terms of thermal history and preservation. First, MIL 03346 contains the most intercumulous, i.e., groundmass, material of any nakhlite, 20–30 vol% (Day et al. 2006; Imae and Ikeda 2007). Second, MIL 03346 is the least affected by post-igneous processes including low-temperature alteration and shock (Treiman 2005). Both features make MIL 03346 particularly well suited for a textural study of groundmass phases. Third, the groundmass appears to represent crystallization in the most oxidizing magmatic environment of all the nakhlites: the groundmass phase assemblage contains fayalitic olivine, titanomagnetite, and a silica phase (Day et al. 2006), indicating proximity to the quartz-fayalite-magnetite oxygen fugacity buffer (Rutherford et al. 2005; Day et al. 2006); the Ti/Al ratio in Ca-pyroxene phenocrysts is similar to experimental samples crystallized at fO_2's ranging between the QFM and NNO buffers (Hammer and Rutherford 2005); the bulk rock has an extremely high Fe^{3+}/total Fe ratio (Dyar et al. 2005), although Domeneghetti et al. (2006) obtain lower values for pyroxene cores. Most relevant for the present purposes, MIL 03346 appears to be the fastest-cooled of all nakhlite magmas (Imae and Ikeda 2007). Treiman (2005) cites evidence for rapid cooling rate of MIL 03346 as: strong normal zoning in the outermost tens of microns in olivine, high Mg# in the core of olivine phenocrysts, scarce plagioclase in the groundmass owing to delayed nucleation, extreme Fe enrichment in olivine and augite rims suggesting a kinetic limitation to the appearance of titanomagnetite, presence of vitrophyric groundmass, spinifex olivine and skeletal titanomagnetite in the groundmass. A dearth of small Ca-pyroxene crystals is interpreted to reflect arrested

nucleation (Lentz et al. 1999). Largely on the basis of textural and compositional indications of rapid cooling, a shallow intrusive or extrusive volcanic history is envisioned for the nakhlites (Imae and Ikeda 2005; Lentz et al. 2005; Treiman 2005; Day et al. 2006). Magma extrusion is a straightforward means of causing the rapid cooling that apparently characterizes the late-stage magmatic history of the suite. An extrusive history is also inferred by analogy with a terrestrial archean komatiite flow (Arndt 1977) bearing phenocryst cumulate texture and mineralogy strikingly similar to the nakhlites (Lentz et al. 1999).

Taken together, the above features suggest a magmatic history of crystal accumulation followed by rapid cooling under relatively oxidizing magmatic conditions. Thus far, it has not been possible to quantify the cooling rate, or consider whether the cumulate texture is physically compatible with extrusive magma emplacement. In this study previously-reported laboratory dynamic crystallization experiments on Fe-rich, Al-poor basalt (Hammer 2006) are employed as a calibration set to quantify the late-stage igneous cooling history of MIL 03346. Lava emplacement mechanisms consistent with petrologic observations and new textural constraints are discussed.

Relevance of Experimental Data Set

This work is predicated on the assumption that experiments using basalt patterned on other martian meteorites are applicable to interpreting the thermal history of MIL 03346. This assumption rests on (a) a close match between the compositions of the experimental starting material and the melt in equilibrium with the cores of MIL 03346 phenocrysts, (b) starting material preparation steps that simulate the relevant melt in the MIL 03346 magma, (c) run conditions that are relevant to the crystallization environment inferred for MIL 03346 from independent studies, and (d) similarities among experimental and MIL 03346 pyroxene compositions.

The composition of the MIL 03346 matrix (i.e., intra-phenocryst melt) has been determined from fusion experiments on portions of the MIL 03346 meteorite (Rutherford and Hammer 2008). Pertinent matrix and melt inclusion compositions from the fusion experiments, along with the experimental starting material composition, are presented in Table 1 and Fig. 1. As clinopyroxenites, the nakhlites fall toward the high Ca/Si extreme of the SNC whole rock classification diagram (Fig. 1). The starting material is low in Ca/Si compared to the nakhlite whole rock field. However, it does fall near the augite-controlled differentiation trend evidenced by several computed nakhlite parent magma compositions (Kaneda et al. 1998; Harvey and McSween 1992a, 1992b; Treiman 1993; Treiman and Goodrich 2001), MIL 03346 whole rock (Anand et al. 2005), and fusion-derived groundmass compositions (Rutherford and Hammer 2008). The starting material is similar to the fusion-derived MIL 03346 groundmass composition, Na-4 (Table 1) in most respects except MgO and to a lesser extent SiO_2 (also apparent in Fig. 1); the CIPW norms of both materials are dominated by pyroxenes (44–58 wt%) and plagioclase (~30%). The starting material also resembles the fusion-derived composition and other Mars meteorites in being Fe-rich and Al-poor compared to terrestrial basalts of similar silica and magnesia contents (Fig. 2). A significant difference between the experimental starting material and the fusion-derived MIL 03346 compositions is higher MgO content of the starting material. While this certainly influences the Mg# of mafic phases in the experiments, it is not expected to have a significant effect on growth kinetics of synthetic phases compared to the natural basalt from which MIL 03346 is derived. Detailed study of olivine forming in the synthetic simple CaO-MgO-Al_2O3-SiO_2 system (e.g., Faure et al. 2003) compares favorably with kinetics of olivine crystallization in natural basalt (e.g., Faure and Schiano 2004).

The details of experimental starting material preparation, mitigation of Fe-loss to capsule material, and the homogenization procedures are provided in Hammer (2006). The relevant issue with respect to this comparative study is whether the thermal treatment of the starting material produced a silicate melt similar in structure to the natural MIL 03346 groundmass melt so that the crystallization response, specifically the nucleation rate of pyroxene during cooling, is similar. While it is impossible to characterize the MIL 03346 melt prior to groundmass crystallization, two lines of evidence suggest that the experimental procedure facilitates the comparison. First is avoidance of extreme and prolonged superheating, which inhibits nucleation when the temperature is reduced below the liquidus (Sato 1995). Most of the starting materials were homogenized at temperatures just slightly above (≤5°) the liquidus temperature determined from equilibrium experiments. This treatment should preclude dissolution of subcritical clusters destined to become crystal nuclei upon cooling (Porter and Easterling 1997). Second, every constant-rate cooling experiment contains ≥40 vol% crystals, with crystallinity more strongly correlated to ambient fO_2 than cooling rate. This suggests that crystallization is inhibited neither by the use of synthetic materials, nor by the initial thermal treatment during fusion and homogenization.

Although the experiments were conceived prior to discovery of MIL 03346 and thus were not tailored to examination of the meteorite's igneous history, the experimental run conditions spanned ranges in cooling rates (2.8 to 230 °C h^{-1}) and oxygen fugacities (corresponding to QFM − 4 to QFM + 5, monitored using solid-medium assemblages of hematite+magnetite, nickel+nickel oxide, quartz+fayalite+magnetite, and iron+wüstite) that likely encompass the crystallization environment of the MIL

Table 1. Compositions of synthetic starting material and estimated MIL groundmass composition.

	MA*[a]	MAm-17[b]	Na-4 matrix[c]
SiO_2	51.4 *(0.8)*	52.0 *(0.3)*	48.5 *(0.26)*
TiO_2	1.63 *(0.09)*	1.64 *(0.04)*	1.39 *(0.08)*
Al_2O_3	9.13 *(0.33)*	7.58 *(0.19)*	8.17 *(0.11)*
FeOT	18.9 *(0.5)*	18.0 *(0.3)*	24.4 *(0.21)*
MgO	7.27 *(0.19)*	7.48 *(0.08)*	3.92 *(0.09)*
CaO	8.77 *(0.21)*	8.15 *(0.04)*	9.51 *(0.14)*
Na_2O	2.13 *(0.09)*	2.45 *(0.05)*	2.38 *(0.05)*
K_2O	0.75 *(0.04)*	0.67 *(0.06)*	0.71 *(0.02)*
MnO	0.00 *(0.00)*	0.52 *(0.07)*	0.53 *(0.05)*
P_2O_5	0.49 *(0.05)*	0.33 *(0.04)*	0.70 *(0.05)*
Cr_2O_3	0.00 *(0.00)*	N.A.	0.03 *(0.01)*
Total	100.4	98.83	100.3
CIPW norm			
Plagioclase	31.1	28.8	29.6
Orthoclase	4.4	4.0	4.2
Diopside	22.8	26.0	28.6
Hypersthene	35.3	36.7	17.8
Olivine	2.3	0.5	15.6
Ilmenite	3.1	3.2	2.6
Magnetite	0.0	0.2	0.1
Apatite	1.1	0.8	1.7

[a]Starting material for constant-rate cooling experiments.
[b]Starting material for variable-rate cooling experiment.
[c]Fusion-derived matrix composition (Rutherford and Hammer 2008).

03346 magma (Lentz et al. 1999; Dyar et al. 2005; Treiman 2005; Mikouchi et al. 2006). The influence of fO_2 on experimental pyroxene composition determined by Hammer (2006) corroborates independent findings that the natural groundmass crystallized at moderately oxidizing conditions (Dyar et al. 2005). This is because reducing conditions (<QFM-3) stabilize feldspar and destabilize Fe-Ti oxides, leading to high Ti/Al (0.40 ± 0.053) in the pyroxenes. In contrast, highly oxidizing conditions lead to high melt Fe^{3+} / Fe^{2+} and abundant Fe-Ti oxides. The Ca-pyroxene formed at ≥QFM + 5 are Mg-rich and have low Ti/Al (0.15–0.17). Moderately oxidizing conditions (QFM + 1 and QFM) produce Ca-pyroxene Ti/Al ratios (0.19 ± 0.021 and 0.21 ± 0.053, respectively) that are most similar to the MIL 03346 Ca-pyroxene (~0.18) (Rutherford, unpublished data; Treiman 2005).

Quantitative Textural Approach

Ca-pyroxene is the phase selected for quantitative textural analysis for several reasons. Most importantly, Ca-pyroxene is the modally dominant mineral in the experimental material and the MIL 03346 groundmass. This facilitates measurements in both materials having reasonable accuracy and precision using standard image analysis techniques. Another advantage is the large variation of the three-dimensional (3D) surface area to volume ratio (having units of area per volume, mm^{-1}, as defined in the next section) with cooling rate, i.e., the morphology is sensitive to cooling rate as an experimental variable. While the 3D aspect ratios of other phases do respond to variations in cooling rate, they are not as extreme as those of pyroxenes (Hammer 2006). Finally, the 3D aspect ratios of pyroxene crystals correlates with qualitative morphology more consistently than those of olivine and titanomagnetite. For example, titanomagnetite crystals characterized as euhedral on the basis of faceted, convex, compact morphologies, may possess ratios exceeding 2000 mm^{-1} due to fine grain size, while large skeletal crystals have 3D aspect ratios as low as 350 mm^{-1}. In contrast, all pyroxene crystals characterized as euhedral have 3D aspect ratios <1000 mm^{-1}, while all anhedral morphologies have values exceeding 1000 mm^{-1}. Further details are available in Hammer (2006).

It must be noted that the coarse-grained Ca-pyroxene population in the calibration set differs fundamentally from the Ca-pyroxene overgrowth rims in MIL 03346. The crystals in the calibration experiments formed by nucleation from the melt, whereas the rims in MIL 03346 represent growth of existing substrate crystals. A meaningful comparison requires that the final textures of both populations be governed by the kinetics of crystal growth rather than crystal nucleation. That is, the magnitude of thermodynamic affinity represented by the existing crystal-melt interface morphology must be similar in each case, as well as small compared to a nucleation-dominated crystallization regime (discussed in Hammer and Rutherford 2002). Planar faceted crystal-melt interfaces and low surface area to volume ratios, which are present in both groups of crystals, are generally accepted to

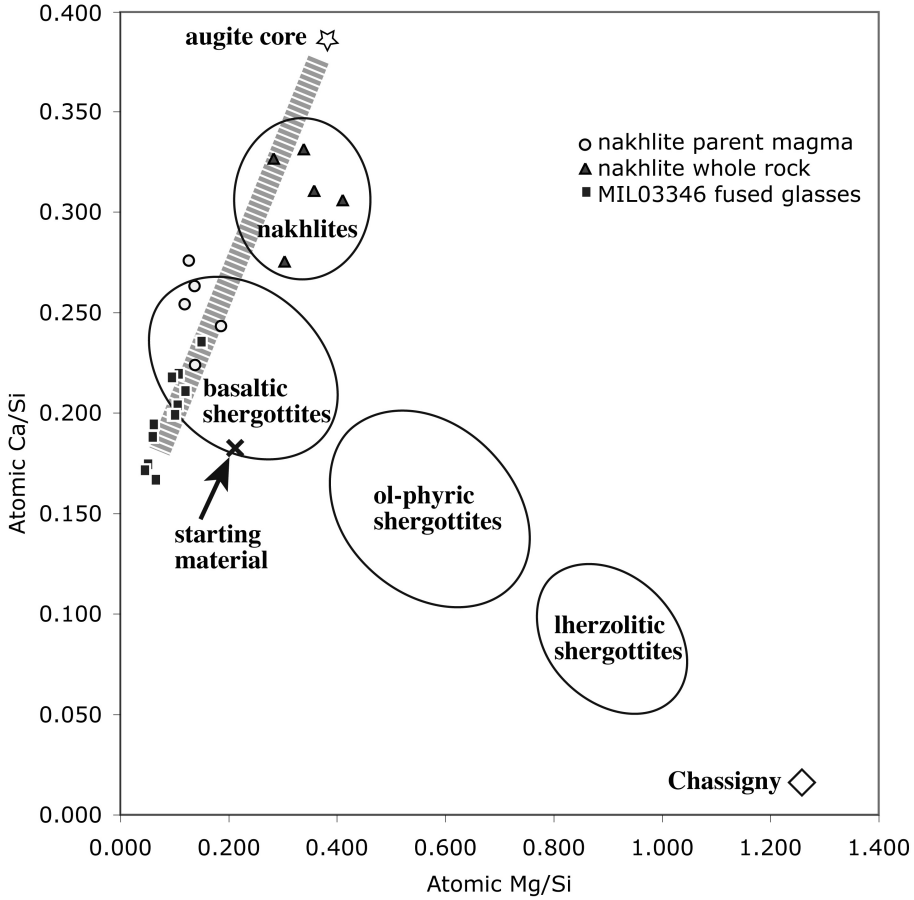

Fig. 1. Meteorite classification diagram (McSween 2007) showing representative MIL 03346 augite core (Treiman 2005), proposed nakhlite parent magmas (Harvey and McSween 1992a, 1992b; Kaneda et al. 1998; Treiman and Goodrich 2001; Treiman 1993), MIL 03346 fused melt inclusion and matrix glasses (Rutherford and Hammer 2008), and nakhlite whole rocks (Treiman 2005). Shaded gray bar indicates differentiation by augite fractionation. Position of Chassigny and meteorite fields from McSween (2007).

represent growth at small to moderate undercooling (Lofgren 1974). To a first order, the comparison between the natural and experimental textures is deemed justified. A small difference in crystallization mechanism may account for the range in cooling rates that produces the phenocryst and groundmass crystal textures of MIL 03346.

METHODS

The 3D aspect ratio, or surface area per unit volume of a pyroxene population (abbreviated S_v^P), is stereologically related to the density of phase boundary intersections in a given length of test line (N_L) and the volume fraction of the phase (ϕ) as:

$$S_v^P = 2N_L/\phi \quad (1),$$

Underwood (1968). The general method of determining N_L is illustrated in Fig. 4.

Thin sections MIL 03346,105 and, 94 were acquired for quantitative image analysis. Sections were viewed in backscatter-electron mode and with energy-dispersive spectrometry in the JEOL 5900LV SEM at the University of Hawaii. Images collected at magnifications of 100, 150, 200, 500, 1000, and 1500× were acquired and analyzed to determine the mode and 3D aspect ratios of pyroxene crystal populations. High resolution digital images of regions nested between phenocrysts were analyzed using Adobe Photoshop and NIH Image J software according to methods described in Hammer (2006). Briefly, circular test lines are digitally overlain on the grayscale BSE images. Locations where crystal-melt boundaries intersect the test line are manually identified and marked using Photoshop tools. Next, the quantity of marked boundary intersections per unit length of test line (N_L) is tabulated by Image J. The area fraction of pyroxene crystals is presumed equivalent to the volume fraction (ϕ; Hilliard 1968), and is measured in Image J by thresholding the characteristic range of grayscale values. The 3D aspect ratio is then found from the measured N_L and ϕ, according to Equation 1.

This usage of the term “aspect ratio” is distinct from previous textural studies (e.g., Saar et al. 2001; Morgan and Jerram 2006), which describe morphology using ratios of the

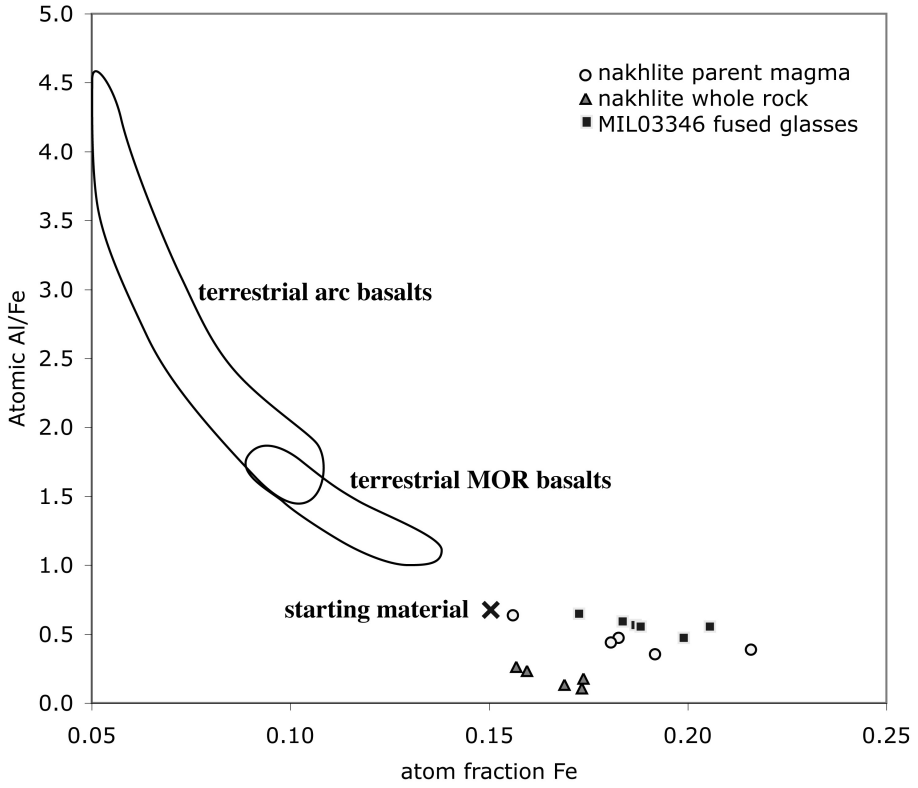

Fig. 2. Iron and aluminum contents of terrestrial arc basalts (Leeman et al. 1990; Wagner et al. 1995; Kinzler et al. 2000), terrestrial MOR basalts (Flower et al. 1982; Peng et al. 1998), and Nakhla derivatives (cited in Fig. 1). All basalts contain 47–53 wt% SiO_2 and 3–7 wt % MgO.

short, intermediate, and long axis dimensions (S: I: L) of individual crystals measured in planar section. The method described here is a population-based statistic and thus does not require delineation of individual crystals. It is especially appropriate in cases where crystals are difficult to segment (e.g., because they are intergrown or skeletal). The S_v^P metric is less time consuming to acquire than 2D aspect ratios and crystal-size distributions, facilitating quantification of a larger sample area in the same amount of analysis time.

Sample means and variance are assessed through evaluation of multiple images, and reported values represent data combined from at least four, and typically eight, images. Where multiple magnifications are employed in characterizing a sample, the values obtained from individual images are weighted. The weighting factor for N_L is the fraction of the total test line length contributed by a given image, and the ϕ values are weighted by the fraction of total specimen area contained in the image. Thus, data from low-magnification images are weighted more heavily than data from high-magnification images in computing sample means, because they subtend a larger specimen area and contain a greater length of test line. Uncertainty in 3D aspect ratio is assessed from the square root of the variance in N_L and ϕ, as propagated through the quotient of Equation 1. This 1σ variation is calculated slightly differently from the method used in Hammer (2006). The NNO and QFM data sets reported here are recalculations. In addition, 25 new images from the NNO series were analyzed to improve measurement statistics.

REVIEW OF PREVIOUS WORK

A review of salient textural results from the previous experimental study (Hammer 2006) provides a framework for textural analysis of MIL 03346. We focus here on the experiments performed at the QFM and NNO buffers because these are deemed relevant to the late stage cooling environment of MIL 03346. The main conclusions do not change if experiments at more and less oxidizing conditions are included because, as explained below, pyroxene 3D aspect ratio is chiefly controlled by cooling rate.

Crystal morphology, apparent crystal size, spatial relationships among phases, and even major element compositional zonation patterns are strongly influenced by cooling rate. In many runs it is possible to distinguish groups of crystals sharing similar characteristics, with each group interpreted as crystals nucleated together and subsequently grown in response to similar magnitudes of undercooling. These groups are distinguished within a given run as separate populations. Three observations from the experiments are central to the present study. First is the presence of porphyritic textures, as exemplified in pyroxene binary images (Figs. 3A–F). As described by Walker et al. (1976) among others, the development of large phenocrysts surrounded by finer-

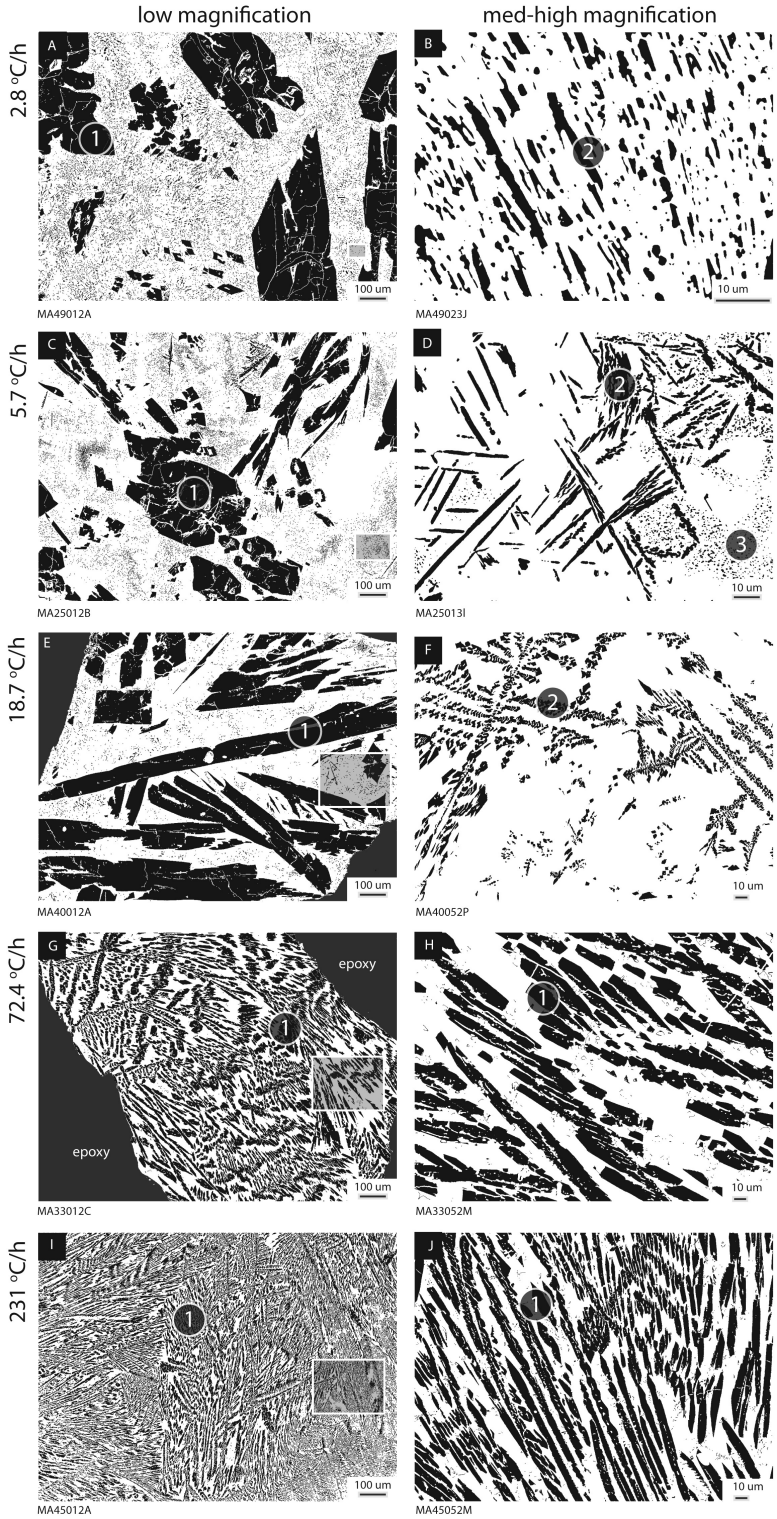

Fig. 3. Minimally processed binary images generated by grayscale thresholding of BSE images of samples run at the NNO buffer. Cooling rate increases downward in each column. The shaded box near the lower right corner of each low-magnification binary image subtends the area of the corresponding medium or high magnification image in the right column. Pyroxene is shown in black; panels E and G contain regions of epoxy (also black). Numbers in circles identify one to three morphologically distinct populations of pyroxene crystals in each run product, where (1) is faceted phenocrystic, (2) is interstitial or dendritic, and (3) is heterogeneously distributed and too fine-grained to resolve with SEM. Samples cooled faster than 19 °C h^{-1} have only one quantifiable population, whereas slower-cooled samples contain at least two populations.

grained groundmass crystals does not require a multistage cooling history but can arise by sequential nucleation events during constant-rate cooling. Second, multiple pyroxene populations, and thus multiple nucleation events (see numbered populations in Fig. 3), occur only if the cooling rate is <72 °C h^{-1}. Third, the 3D aspect ratios of separate pyroxene populations progressively diverge as cooling rate decreases (Fig. 5A). This trend in textural dispersion results in the slowest-cooled materials containing populations having both the lowest and highest observed 3D aspect ratios, while moderately-cooled experiments contain two morphologically similar populations, and fastest-cooled experiments contain only one population. The logarithm of the cooling rate is linearly related to the logarithm of the population 3D aspect ratio (Fig. 5A), with the coarse-grained population decreasing by two orders of magnitude and the fine-grained population doubling over the cooling rate range examined. A third population of pyroxene crystals occurs in several run products (e.g., Fig. 3D). Quantitative analysis of these populations is not presented because crystals are heterogeneously distributed, difficult to spatially resolve, and inconsistently present among runs cooled at the same rate.

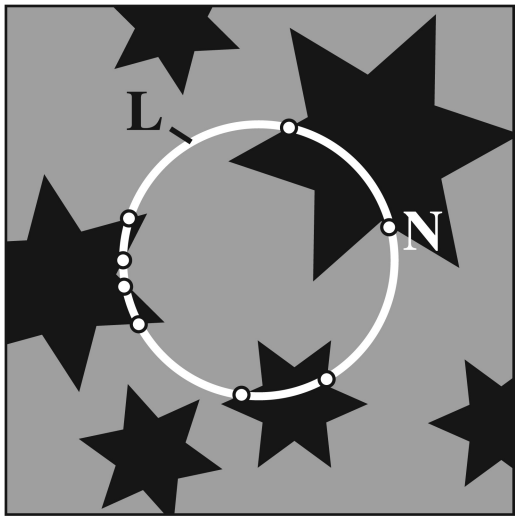

Fig. 4. Schematic representation of textural analysis method for determining N_L. A test line, L (white circle), is overlain on an arbitrary sample plane. The locations where the test line intersects the boundaries between phases (black stars and gray matrix) are marked and tabulated. A large number of test lines from many images are used to determine the average number of intersections per unit length of test line, N_L. The interface area per unit volume of a phase is given by $\boldsymbol{S_v} = 2N_L$, and the surface area per unit volume of the phase, $\boldsymbol{S_v^P}$, is $\boldsymbol{S_v}/\phi$ (Underwood 1968).

RESULTS

Pyroxene Populations in MIL 03346

Although the cores of Ca-pyroxene phenocrysts in MIL 03346 are compositionally uniform and relatively homogeneous (En_{38} Wo_{42}), the outer rims of all crystals are strongly zoned, extending to $En_{06}Wo_{51}$ (McKay et al. 2005; Treiman 2005). As discussed below, the formation of homogeneous cores and strongly zoned rims occur under different conditions, perhaps separated by eruption or the onset of crystal settling in a stagnant lava pile. Following recent precedent (Day et al. 2006), zoned rims are interpreted to have formed at the onset of groundmass crystallization, and thus phenocryst rims are considered part of the groundmass. The rims are analyzed as a distinct crystal population, and the 3D aspect ratio determined from the phenocryst-groundmass interface reflects the growth morphology of euhedral crystals. A second distinctive pyroxene population occurs in the groundmass as externally faceted, tabular to hopper microphenocrysts 10–20 microns long. A third population of very fine-grained pyroxene, decorated with Fe-Ti oxides and occurring in a gridwork pattern, is also discernible. Representative examples of the three populations are apparent in the nested BSE grayscale images and corresponding pyroxene binary images of Fig. 6. Unfortunately, quantitative analysis of the third population of pyroxene is hindered by the extremely fine grain size and shared grayscale range with Cl-phosphate. Also challenging is the intergrowth with oxides that complicates determination of 3D aspect ratio, since this is defined by the crystal-melt interface. We note that even if these challenges could be surmounted, a quantitative interpretation is precluded by the presence of just two populations in the calibration set (recalling that a third population is not quantified due to its heterogeneous spatial distribution).

Cooling Rate of MIL 03346 Groundmass

A linear relationship on a plot of log cooling rate (°C h^{-1}) versus log 3D aspect ratio (mm^{-1}) established in the QFM and NNO constant-rate cooling experiments (Fig. 5A) is used to quantitatively constrain the MIL 03346 groundmass cooling history preserved in the textures of phenocrysts and microphenocrysts (Fig. 5B). The phenocryst 3D aspect ratio in MIL 03346 determined from analysis of 13 BSE images (corresponding to 11.3 mm^2) is 112 mm^{-1} (1σ = 8.3 mm^{-1}). This value is reproduced in the low 3D aspect ratio population of the experimental calibration set at an interpolated cooling rate of 9.5 °C h^{-1}. Maximum and minimum cooling rate estimates are obtained by comparing extremes in the 1σ error envelopes of the calibration set with overlapping variation in the MIL 03346 phenocryst population, yielding 22 and 5.0 °C h^{-1}, respectively. The mean 3D aspect ratio of the microphenocryst population in MIL 03346,1530 mm^{-1} (1σ = 160), matches the high 3D aspect ratio population of synthetic crystals formed at cooling rates above 17 °C h^{-1}. However, extension of the second population trend lines above 19 °C h^{-1} is uncertain, because no run cooled faster than 19 °C h^{-1} exhibited more than one population. That is,

the maximum cooling rate at which a second nucleation event occurs is constrained to lie between 19 and 72 °C h^{-1}. Therefore, the maximum cooing rate range shown in Fig. 5B for MIL 03346 (5.0–120 °C h^{-1}), which utilizes the full uncertainty envelope given by variance in the calibration set and MIL 03346 groundmass, is not plausible. The range of cooling rates at the intersection of both experimental populations with the MIL 03346 phenocrysts and microphenocrysts is quite narrow: 17.4–21.7 °C h^{-1}, or approximately 20 °C h^{-1}.

DISCUSSION

Constant Rate Cooling in a Geologic Context

As described above, the dynamic crystallization experiments utilized in Hammer (2006) impose a constant cooling rate on starting materials initially near the liquidus temperature. This is a standard type of cooling experiment (Lofgren 1980; Wyllie et al. 1981) because it is simple to execute with programmable furnace power controllers. In addition, because the cooling rate history does not vary arbitrarily, the results are not tied to a specific magma reservoir geometry or heat flow mechanism. Despite being comparatively general, the thermal profiles of constant-rate or linear cooling experiments have the disadvantage of not simulating natural cooling profiles. Linearly decreasing temperature is a poor approximation of natural magma cooling, since heat transfer rates vary with the difference in temperature between the magma and surroundings, leading to strongly decreasing rates of cooling over time. An implicit assumption of the constant-rate cooling approach is that a suite of constant-rate cooling runs spanning at least an order of magnitude in rate probably captures essential differences in the progress of crystal nucleation, crystal growth, and melt differentiation. While a full exploration of the assumption is beyond the scope of this study, it is provisionally evaluated with a variable rate (VR) cooling experiment.

The thermal profile computed by Bowles et al. (Forthcoming) at an arbitrary distance (0.25 m) below the surface of a cooling basaltic lava flow provides a reasonable comparison with the suite of constant rate (CR) cooling experiments. The temperature-time path for basalt starting at 1250 °C was calculated numerically using a solution to the conductive heat flow equation that includes propagation of a solidified layer (i.e., incorporates release of latent heat) into a constant-temperature half-space. That is, the Stefan problem is solved using the method of Turcotte and Schubert (1982) with reasonable values for basalt thermophysical properties: specific heat 0.84 kJ kg^{-1} K^{-1}, thermal diffusivity 1 mm^2 s^{-1}, thermal conductivity 2 J m^{-1} s^{-1} K^{-1}, density 2950 kg m^{-3}, latent heat of fusion 320 kJ kg^{-1}, and temperature at the boundary 0 °C). The resulting thermal profile was discretized into 28 constant-rate cooling ramp segments (Fig. 7) for input to a Eurotherm 2404 temperature controller. The starting material used in the variable-rate (VR) experiment (Bowles et al. 2007; Bowles et al., Forthcoming) is similar to the batch used in the CR calibration set (Table 1). The experiment is performed at the QFM buffer, and sample preparation and analysis techniques are similar to those described in Hammer (2006). Several points of comparison between the CR experiments and VR experiment are considered: (a) Early, high-temperature segments of the VR experiment have cooling rates near the upper end of rates used in the CR set (near 72 °C h^{-1}). (b) Both the VR experiment and the CR experiments at moderate cooling rate (19 °C h^{-1} °C h^{-1}) reach 600 °C after the same run time (i.e., they have the same average cooling rate above this temperature). (c) The low-temperature segments of the VR experiment are similar to the rate imposed in the slowest-cooled CR experiment (5.7 °C h^{-1}). Textural similarity of the VR run product with one of these CR experiments would indicate dominance of the high, middle, or low-temperature portion of the VR cooling curve, respectively, and suggest the appropriate analogy between CR experiments and natural conductive cooling.

Qualitative and quantitative results are shown in Fig. 8 and 9. A key outcome is that only a single pyroxene population is present in the VR run product. By similarity with the CR experiments, this is interpreted as a lack of time for a second population to nucleate and grow to visible size (Hammer 2006). This indicates dominance of the early, rapid-cooling portion of the thermal profile in controlling pyroxene texture in the VR experiment. Quantitatively, the 3D aspect ratio of the VR crystals correlates with the CR trend at ~150 °C h^{-1}, with a total range in 3D aspect ratio including heterogeneity and uncertainties in the calibration set of 67–270 °C h^{-1} (Fig. 9). The lower end of this range approaches the actual maximum cooling rate applied in the VR run (53 °C h^{-1}). This pilot experiment indicates that constant-rate cooling experiments can produce textures similar to those generated by geologically realistic thermal histories. It further suggests that the textures of constant-rate experiments be interpreted as reflecting crystallization at the *onset* of natural magma cooling.

Applying the results from the VR experiment to our findings from the MIL 03346 texture (Fig. 5B), the constant-rate cooling range estimated for MIL 03346 (~20 °C h^{-1}) is interpreted to represent the initial rate of temperature change experienced by the crystallizing groundmass melt. If the MIL 03346 magma cools conductively according to the model described above, the cooling rates obtained from pyroxene textures represent crystallization at a depth of ~0.4 m below the surface of the lava. Reasonable variations in the thermophysical parameters impose only a minor effect on the computed

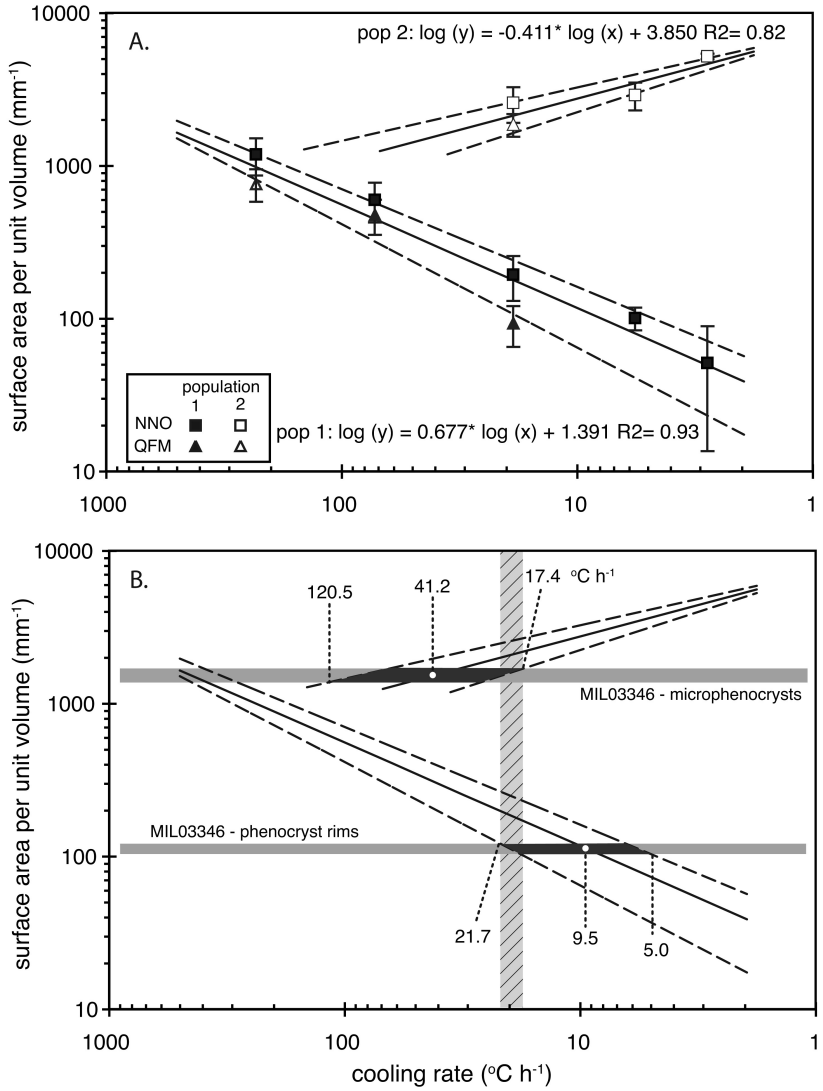

Fig. 5. Quantitative relationship between cooling rate and pyroxene texture. Abscissa axis values increase toward the left so that the reversibility of the solidification process, and thus the approach to textural equilibrium, increases to the right. A) Long dashed lines are least squares fits to 1σ variance about sample means. Extension of second population trend lines to cooling rates above 19 °C h^{-1} is for illustrative purposes only; symbol positions show that no experiment cooled faster than 19 °C h^{-1} contained a second crystal population. B) Linear trends from experimental data set are overlaid by clinopyroxene populations in MIL 03346 as shaded horizontal bars. Because two populations are observed, the maximum calculated cooling rate must be less than 72 °C h^{-1}. Vertical shaded bar shows cooling rate range that satisfies texture of both phenocryst rims and microphenocrysts (17.4–21.7 °C h^{-1}, or ~20 °C h^{-1}).

depths. For example, setting boundary temperature = 150 °C decreases the depth range by <5 cm. Thus, the very rapid late-stage cooling of the MIL 03346 groundmass constrains the lava body to at least 0.8 m total thickness, but does not require extreme thicknesses (≥30 m) proposed in previous studies (Mikouchi et al. 2006).

Multiple Nucleation Events

The observation of multiple populations of distinctive morphologies and 3D aspect ratios in the experimental calibration set suggests an alternate explanation for the dearth of small phenocrysts in the meteorite (Lentz et al. 1999). This feature of the crystal size distribution has been interpreted as the result of cessation of nucleation or crystal resorption (Lentz et al. 1999; Treiman 2005), both explanations suggesting destabilization of pyroxene late in the crystallization history of the groundmass. The presence of extremely fine grained pyroxene in the groundmass of MIL 03346, coupled with a dearth of crystals in the microphenocryst range may actually reflect buildup of thermodynamic affinity necessary to drive a second (and even third) nucleation event. Inspection of textures such as those shown in Figs. 3A–F suggests that discontinuities in the size distribution exist between morphologically distinct populations, which we have interpreted as representing

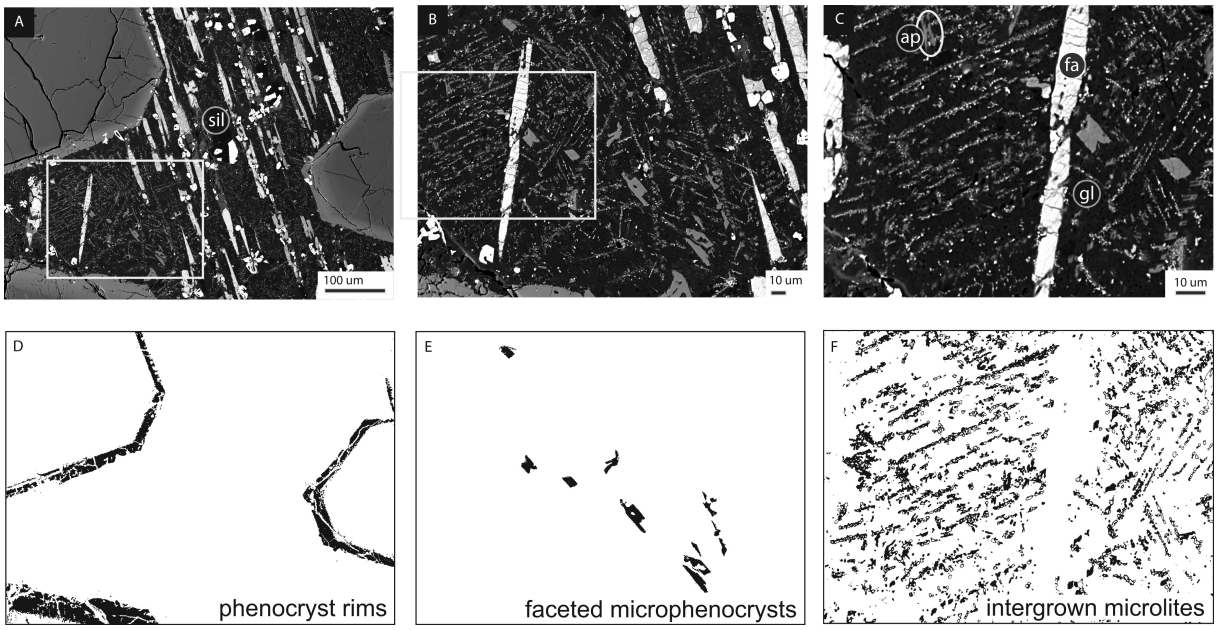

Fig. 6. BSE images of MIL 03346,105 at three magnifications (A, B, C). White box in panels (A) and (B) outline the areas shown in images (B) and (C), respectively. Three morphologically distinct populations of clinopyroxene are selected by thresholding and image processing (to distinguish clinopyroxene from chlorapatite) to create binary pyroxene maps (D, E, F). The three populations are: (D) faceted outermost growth zones of phenocrysts, (E) faceted compositionally homogeneous microphenocrysts, and (F) anhedral microlite crystals intergrown with titanomagnetite. Other phases present are fayalitic olivine (fa), chlorapatite (ap, circled in c), silica (sil) and glassy mesostasis (gl). Cracks (e.g., apparent in D) were ignored in image analysis and 3D aspect ratio determination.

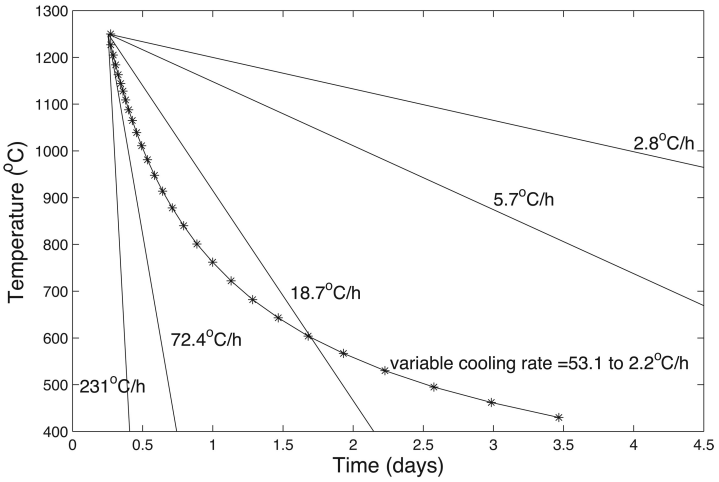

Fig. 7. Variable-rate and constant-rate cooling profiles included in the textural calibration set.

discrete nucleation events. Multiple nucleation events are in fact expected if spikes in affinity accompany the appearance of new phases (particularly those that reject components taken up by pyroxene); growth of these phases causes constitutional undercooling (Dowty 1980) of pyroxene in the surrounding melt.

Physical Environment of MIL 03346 Magma Emplacement

In concert, extreme phenocryst accumulation (to 70–80 vol%) and the late-stage cooling rate (~20 °C h^{-1}) determined here pose constraints on the igneous history of MIL 03346. Emplacement and cooling of the MIL 03346 magma as a sill or dike (Imae and Ikeda 2005; Treiman 2005) is not considered reasonable in view of this cooling rate. It is generally accepted on the basis of compositional zoning patterns that the cores of pyroxene and olivine phenocrysts crystallized in an environment of low crystal/melt ratio, and that the rims crystallized after crystal accumulation in an oxidizing environment of high crystal/melt ratio (Day et al. 2006). Taking MIL 03346 augite and olivine phenocryst core compositions (Treiman 2005), proposed parent magma

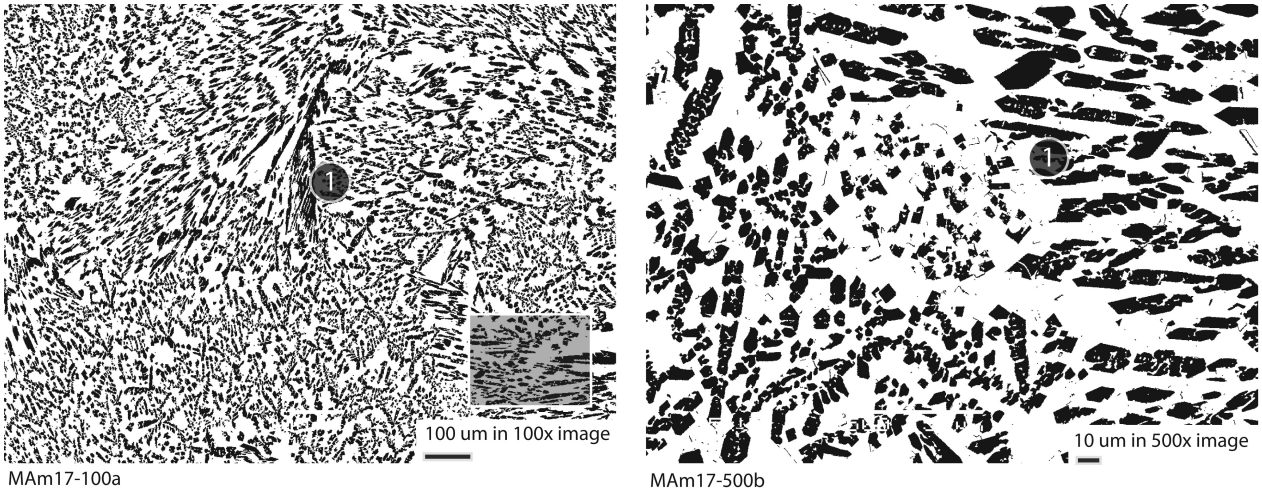

Fig. 8. Binary images of the single pyroxene population generated in the variable-rate cooling experiment. Definitions are as in Fig. 3.

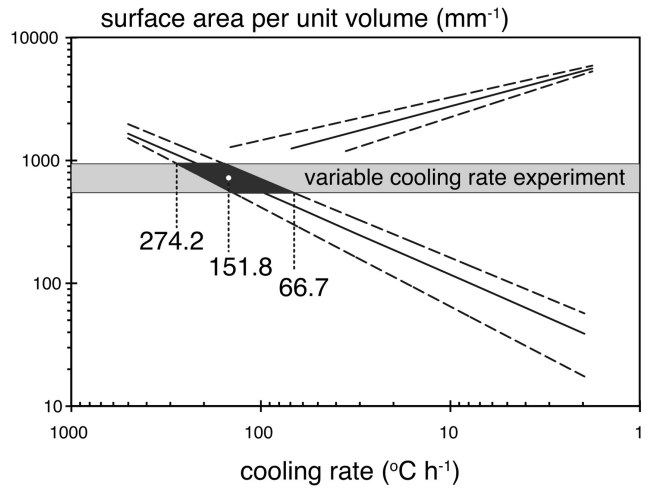

Fig. 9. Linear trends from experimental data set are overlaid by clinopyroxene populations in MIL 03346 as a shaded horizontal bar. A single population of relatively high 3D aspect ratio crystals indicates that pyroxene texture in the VR run is most sensitive to the early, rapid cooling portion of the experiment.

compositions (Harvey and McSween 1992a, 1992b; Treiman 1993; Kaneda et al. 1998; Treiman and Goodrich 2001), and the fusion-derived Na-4 (Table 1) as the composition of the melt in equilibrium with the phenocryst cores, simple mass balance calculations indicate that the magma contained 80–93 wt% melt prior to crystal accumulation. Thus, the crystal accumulation process essentially inverted the crystal:melt ratio. Models differ as to whether the transition from melt-dominated to crystal-dominated regimes occurs prior to or following extrusion to the Mars surface.

One end member model is eruption of crystal-poor magma having bulk composition equivalent to the parent magma, developed by analogy with the texturally similar Archean ultramafic Theo's Flow (Lentz et al. 1999). Crystals may nucleate in a cool upper boundary zone, cluster together, and be carried to the base of the lava flow or lake by convection currents. This model accounts for clustering of crystals in the cumulate (Day et al. 2006; Lentz et al. 1999) and the homogeneity of crystal size distributions among nakhlites, which could represent different portions of the convecting lava core. Mikouchi et al. (2006) imply that crystal accumulation occurred after magma emplacement, in their calculation of depths into a lava body represented by each nakhlite using diffusional relaxation of Ca chemical potential gradients in olivine phenocrysts (Mikouchi and Miyamoto 2002a; Mikouchi et al. 2006) following methods of Mikouchi and Miyamoto (2002b). Listed in order of increasing subsolidus cooling rate and correspondingly decreasing depths into the lava, the meteorites are Northwest Africa (NWA) 998/ Lafayette, Nakhla/ Governador Valadares, Yamato (Y-) 000593, MIL 03346, and NWA 817. A problem with this model is that melt residual to in situ pyroxene crystallization would be of lower density than the crystals and form an upper zone of differentiated melt that is not accounted for in calculations of the meteorite depths of origin, e.g., ≤4 m for MIL 03346 (Mikouchi et al. 2006). In fact, a large volume of the nakhlite parent magma must be residual to formation of the cumulates. Evolved rocks representing this expelled interstitial liquid are notable by their absence from the Mars meteorite collection.

Assuming that pyroxene and olivine accumulation occurred post-eruptively (Day et al. 2006), terrestrial analogs and our proposed late-stage cooling rate suggests inflated pahoehoe sheet inflation as a likely mechanism of lava emplacement. On Earth, pahoehoe lava flowing on shallow slopes may develop into broad sheets by coalescence of lava toes that break out from cracks in the crust of the advancing flow front (Hon et al. 1994). The core of an initially thin (10s of cm) sheet flow remains molten as the flow inflates, impounded by a thickening viscoelastic crust. Sheets may reach thicknesses of 10s of m, e.g., (Kauahikaua et al. 1998;

Thordarson and Self 1993), if the magma supply rate is sufficient to overcome frictional resistance of separating the upper and lower crusts (Kilburn 2000). Due to lower viscosity, the proposed nakhlite parent melts (Harvey and McSween 1992b; Treiman 1993) would provide 3.5–10 times less resistance than typical terrestrial tholeiite, according to the viscosity calculation method of Shaw (1972). Additionally, pahoehoe lava may travel great distances and cover broad areas if confined in tubes (Ho and Cashman 1997; Self et al. 1998). The heat loss from pahoehoe interiors is dominantly conductive after the first few seconds (Keszthelyi and Denlinger 1996), leading to distinctive crystal textures in which grain sizes coarsen inward from flow tops and bases (Katz and Cashman 2003). A'a, by contrast, is stirred continuously, cooled radiatively, and characterized by high rates of crystal nucleation and uniformly fine crystal size (Cashman et al. 1999). Finally, the lower gravity of Mars relative to Earth reduces the rate of flow advance for a given supply rate. This promotes greater heat loss per unit distance traveled and formation of a thicker insulating crust (Rowland et al. 2004). On shallow slopes, these factors would favor emplacement of low-viscosity basaltic lava as inflated pahoehoe sheets rather than channelized pahoehoe or a'a.

A more plausible scenario suggested by analogy with terrestrial shield tholeiites is that crystal accumulation begins in a subsurface reservoir and continues after surficial emplacement. Olivine rich (i.e., picritic) basalt flows with crystal contents exceeding 15 vol% at the vent constitute ~14% of exposed flows on Mauna Loa (Mueller et al. 2004). Picrites from the 1852 and 1868 eruptions of Mauna Loa are interpreted as a combination of deep-seated crystal mush mixing with more typical shallow reservoir material (Rhodes 1995). On Mauna Loa, entrainment and suspension of high crystal concentrations may require high magma supply rate and unusually vigorous magma column dynamics (Rhodes 1995; Gaffney 2002; Mueller et al. 2004). Consistent with this inference, vents on the rift zones and flanks of both Kilauea and Mauna Loa produce crystal-rich magma more frequently than do summit vents (Trusdell, personal communication) Most importantly, crystal accumulation by settling occurs at the bases of picritic pahoehoe flows of Mauna Loa and Kilauea, with crystallinities commonly reaching 50 vol% (Trusdell, personal communication) Again, a'a behaves quite differently, because crystal settling is inhibited by the internal stirring associated with this flow type; phenocryst cumulates are not observed in a'a flows.

Again by analogy with terrestrial picrites, lava issuing from the nakhlite lava source vent could be quite pyroxene-rich with a bulk composition intermediate between that of the meteorite and its parent magma. Since a mush of dominantly solid particles would be uneruptable except as a plug or spine (Lavallee et al. 2007), the extremely high crystallinities of the nakhlites suggests that some crystal accumulation (and subsequent expulsion of interstitial liquid) occurs after emplacement. While high crystallinities elevate magma viscosity by several orders of magnitude (Pinkerton and Stevenson 1992), cause development of a yield strength (Hoover et al. 2001), and influence the lava emplacement style, flow morphology, and flow length (Crisp et al. 1994; Harris and Rowland 2001), the ability of such magmas to flow in subsurface conduits and erupt is supported by fluid mechanical models of convection in magma containing up to 50 vol% entrained solids (Bachmann and Bergantz 2004). Finally, eruption of magma with appreciable crystal content (a) considerably reduces the problem of the absent residual melt inherent to the in situ crystallization model, since the "missing" melt was never part of the flow, (b) reasonably accounts for the sharp transition between Ca-pyroxene phenocryst cores and rims, if cores were formed prior to eruption in a subsurface reservoir, and (c) is consistent with the possibility that ambient fO_2 is higher during late-stage groundmass crystallization than crystallization of phenocryst cores (Rutherford and Hammer 2008).

CONCLUSIONS

A working hypothesis of physical aspects of the MIL 03346 magma emplacement that meets the constraints on cumulate texture and late-stage cooling rate is emplacement of crystal-rich magma as an inflated pahoehoe sheet. The interior would cool conductively as treated here and previously (Mikouchi et al. 2006), and provide a sufficiently thick molten layer to incorporate crystal settling as described in the general nakhlite formation models of Mikouchi et al. (2006) and Lentz (1999). Breakouts of interstitial melt through cracks in the confining crust allow for the possibility of separate lobes for each of the nakhlites, and even the opportunity for additional crystal concentration in the trunk lobe by filter pressing (Lentz et al. 2005), although to our knowledge this process has not be observed in the picritic flows of Mauna Loa. Physical separation of cumulates from their residual melts, e.g., as proposed for large silicic reservoirs by Bachmann and Bergantz (2004), may explain why materials representing nakhlite residual magma are absent from the meteorite record.

Acknowledgments–Julie Bowles is thanked for fruitful discussions of magma crystallization kinetics. Scott Rowland and Frank Trusdell provided early feedback and discussions of crystal-rich lavas. Jeff Taylor and Julie Stopar are thanked for use of thin section MIL 03346,94. This work benefited from discussions of nakhlites with Malcolm Rutherford and Rachel Lentz. The manuscript was improved with helpful reviews by Dougal Jerram, Takashi Mikouchi, and Allan Treiman. This work was supported by NASA NNG05GL92G, and is SOEST Publication #7510.

Editorial Handling—Dr. Allan Treiman

REFERENCES

Anand M., Williams C. T., Russell S. S., Jones G., James S., and Grady M. M. 2005. Petrology and geochemistry of nakhlite MIL 03346: A new Martian meteorite from Antarctica (abstract #1639). 36th Lunar and Planetary Science Conference. CD-ROM.

Arndt N. T. 1977. Thick, layered peridotite-gabbro lava flows in Munro Township, Ontario. *Canadian Journal of Earth Sciences* 14:2620–2637.

Bachmann O. and Bergantz G. W. 2004. On the origin of crystal-poor rhyolites: Extracted from batholithic crystal mushes. *Journal of Petrology* 45:1565–1582.

Bowles J. A., Hammer J. E., and Brachfeld S. A. 2007. Magnetic and petrographic characterization of synthetic Martian basalts (abstract #3255). Seventh International Conference on Mars. CD-ROM.

Bowles J. A., Hammer J. E., and Brachfeld S. A. Forthcoming. Magnetic and petrologic characterization of synthetic Martian basalts and implications for the surface magnetization of Mars. *Journal of Geophysical Research (Planets)*.

Cashman K. V., Thornber C., and Kauahikaua J. P. 1999. Cooling and crystallization of lava in open channels, and the transition of Pahoehoe Lava to 'A'a. *Bulletin of Volcanology* 61:306–323.

Crisp J., Cashman K. V., Bonini J. A., Hougen S. B., and Pieri D. C. 1994. Crystallization history of the 1984 Mauna Loa lava flow. *Journal of Geophysical Research-Solid Earth* 99:7177–7198.

Day J. M. D., Taylor L. A., Floss C., and McSween H. Y. Jr. 2006. Petrology and chemistry of MIL 03346 and its significance in understanding the petrogenesis of nakhlites on Mars. *Meteoritics & Planetary Science* 41:581–606.

Domeneghetti M. C., Fioretti A. M., Camara F., Molin G., and McCammon C. 2006. Constraints on the thermal history and oxidation state of MIL 03346 Martian meteorite; single-crystal XRD, electron microprobe and Mössbauer analyses of clinopyroxene (abstract #1238). 37th Lunar and Planetary Science Conference. CD-ROM.

Dowty E. 1980. Crystal growth and nucleation theory. In *Physics of magmatic processes*, edited by R. Hargraves, Princeton, New Jersey: Princeton University Press. pp. 487–551.

Dyar M. D., Treiman A. H., Pieters C. M., Hiroi T., Lane M. D., and O'Connor V. 2005. MIL 03346, the most oxidized Martian meteorite: A first look at spectroscopy, petrography, and mineral chemistry. *Journal of Geophysical Research-Planets* 110, doi: 10.1029/2005JE002426.

Faure F., Trolliard G., Nicollet C., and Montel J. M. 2003. A developmental model of olivine morphology as a function of the cooling rate and the degree of undercooling. *Contributions to Mineralogy and Petrology* 145:251–263.

Faure F. and Schiano P. 2004. Crystal morphologies in pillow basalts: Implications for mid-ocean ridge processes. *Earth and Planetary Science Letters* 220:331–344.

Flower M., Pritchard R. G., Brem G., Cann J. R., Delany J., Emmerman R., Gibson I. L., Oakley P. J., Robinson P. T., and Schmincke H. U. 1982. Chemical stratigraphy, Iceland Research Drilling Project Reydarfjordur, eastern Iceland. *Journal of Geophysical Research* 87:6489–6510.

Gaffney A. M. 2002. Environments of crystallization and compositional diversity of Mauna Loa xenoliths. *Journal of Petrology* 43:963–980.

Hammer J. E. and Rutherford M. J. 2002. An experimental study of the kinetics of decompression-induced crystallization in silicic melt. *Journal of Geophysical Research B (Solid Earth)* 107:8-1–8-24.

Hammer J. E. and Rutherford M. J. 2005. Experimental crystallization of Fe-rich basalt: Application to cooling rate and oxygen fugacity of nakhlite MIL 03346 (abstract #1999). 36th Lunar and Planetary Science Conference. CD-ROM.

Hammer J. E. 2006. Influence of fO_2 and cooling rate on the kinetics and energetics of Fe-rich basalt crystallization. *Earth & Planetary Science Letters* 248:618–637.

Harris A. J. L. and Rowland S. K. 2001. FLOWGO: A kinematic thermo-rheological model for lava flowing in a channel. *Bulletin of Volcanology* 63:20–44.

Harvey R. P. and McSween H. Y. 1992a. The parent magma of the nakhlite meteorites—Clues from melt inclusions. *Earth and Planetary Science Letters* 111:467–482.

Harvey R. P. and McSween H. Y. 1992b. Petrogenesis of the nakhlite meteorites- evidence from cumulate mineral zoning. *Geochimica et Cosmochimica Acta* 56:1655–1663.

Hilliard J. E. 1968. Measurement of volume in volume. In *Quantitative microscopy*, edited by R. T. DeHoff and F. N. Rhines, New York: McGraw-Hill. pp. 45–76.

Ho A. M. and Cashman K. V. 1997. Temperature constraints on the Ginkgo Flow of the Columbia River Basalt Group. *Geology* 25: 403–406.

Hon K., Kauahikaua J., Denlinger R., and MacKay K. 1994. Emplacement and inflation of pahoehoe sheet flows—Observations and measurements of active lava flows on Kilauea volcano, Hawai'i. *Geological Society of America Bulletin* 106: 351–370.

Hoover S. R., Cashman K. V., and Manga M. 2001. The yield strength of subliquidus basalts—Experimental results. *Journal of Volcanology and Geothermal Research* 107:1–18.

Imae N. and Ikeda Y. 2005. Comparative petrology of Yamato and MIL 03346 nakhlites (abstract #5058). *Meteoritics & Planetary Science* 40:A72.

Imae N. and Ikeda Y. 2007. Petrology of the Miller Range 03346 nakhlite in comparison with the Yamato-000593 nakhlite. *Meteoritics & Planetary Science* 42:171–184.

Kaneda K., McKay G., and Le L. 1998. Synthetic Nakhla pyroxenes: A close match at last (abstract #1620). 39th Lunar and Planetary Science Conference. CD-ROM.

Katz M. G. and Cashman K. V. 2003. Hawaiian lava flows in the third dimension; identification and interpretation of pahoehoe and aa distribution in the KP^{-1} and SOH^{-4} cores. *Geochemistry, Geophysics, Geosystems—G (Super 3)* 4:24.

Kauahikaua J., Cashman K. V., Mattox T. N., Heliker C. C., Hon K. A., Mangan M. T., and Thornber C. R. 1998. Observations on basaltic lava streams in tubes from Kilauea volcano, Island of Hawai'i. *Journal of Geophysical Research (Solid Earth)* 103: 27303–27323.

Keszthelyi L. and Denlinger R. 1996. The initial cooling of pahoehoe flow lobes. *Bulletin of Volcanology* 58:5–18.

Kilburn C. R. J. 2000. Lava flows and flow fields. In *Encyclopedia of volcanoes*, edited by H. S. Sigurdsson, New York: Academic Press. pp. 291–305.

Kinzler R. J., Donnelly-Nolan J. M., and Grove T. L. 2000. Late Holocene hydrous mafic magmatism at the Paint Pot crater and Callahan flows, Medicine Lake volcano, N-California and the influence of H_2O in the generation of silicic magmas. *Contributions to Mineralogy and Petrology* 138:1–16.

Lavallee Y., Hess K.-U., Cordonnier B., and Dingwell D. B. 2007. Non-Newtonian rheological law for highly crystalline dome lavas. *Geology* 35:843–846.

Leeman W., Smith D., Hildreth W., Palacz Z., and Rogers N. 1990.

Compositional diversity of late Cenozoic basalts in a transect across the southern Washington Cascades: Implications for subduction zone magmatism. *Journal of Geophysical Research* 95:19,561–19,582.

Lentz R. C. F., Taylor G. J., and Treiman A. H. 1999. Formation of a Martian pyroxenite: A comparative study of the nakhlite meteorites and Theo's Flow. *Meteoritics & Planetary Science* 34: 919–932.

Lentz R. C. F., McCoy T. J., and Taylor G. J. 2005. Multiple nakhlite lava flows? (abstract #5298). *Meteoritics & Planetary Science* 40:A91.

Lofgren G. 1974. An experimental study of plagioclase crystal morphology: Isothermal crystallization. *American Journal of Science* 274:243–273.

Lofgren G. E. 1980. Experimental studies on the dynamic crystallization of silicate melts. In *Physics of magmatic processes*, edited by R. Hargraves. Princeton, New Jersey: Princeton University Press. pp. 487–551.

McBride K. M., Righter K., Satterwhite C. E., Schwarz C., and Robinson P. 2005. Curation and allocation of the new Antarctic nakhlite, MIL 03346 (abstract #1499). 39th Lunar and Planetary Science Conference. CD-ROM.

McKay G., Schwandt C., and Code K. 2005. Mineralogy and petrology of new Antarctic nakhlite MIL 03346 (abstract #2351). 36th Lunar and Planetary Science Conference. CD-ROM.

McSween H. Y. Jr. 2007. Mars. In *Meteorites, comets, and planets*, edited by A. M. Davis. Treatise on Geochemistry, vol. 1. Oxford: Elsevier. pp. 1–27.

Mikouchi T. and Miyamoto M. 2002a. Comparative cooling rates of nakhlites as inferred from iron-magnesium and calcium zoning of olivines (abstract #1343). 38th Lunar and Planetary Science Conference. CD-ROM.

Mikouchi T. and Miyamoto M. 2002b. Mineralogy and olivine cooling rate of the Dhofar 019 shergottite. *Antarctic Meteorite Research* 15:122–142.

Mikouchi T., Miyamoto M., Koizumi E., Makishima J., and McKay G. 2006. Relative burial depths of nakhlites: An update (abstract #1865). 37th Lunar and Planetary Science Conference. CD-ROM.

Morgan D. J. and Jerram D. A. 2006. On estimating crystal shape for crystal size distribution analysis. *Journal of Volcanology and Geothermal Research* 154:1–7.

Mueller A., Trusdell F. A., and Rhodes J. M. 2004. Petrology, geochemistry, flow dynamics, GIS mapping and hazards of the Hapaimamo flow, Mauna Loa volcano, Hawai'i (432–433). Geological Society of America.

Peng Z. X., Mahoney J. J., Hooper P. R., MacDougall J. D., and Krishnamurthy P. 1998. Basalts of the northeastern Deccan Traps, India: Isotopic and elemental geochemistry and relation to southwestern Deccan stratigraphy. *Journal of Geophysical Research* 103:29,843–29,865.

Pinkerton H. and Stevenson R. J. 1992. Methods of determining the rheological properties of magmas at sub-liquidus temperatures. *Journal of Volcanology and Geothermal Research* 53:47–66.

Porter D. and Easterling K. 1997. *Phase transformations in metals and alloys*. London: Chapman & Hall. 514 p.

Rhodes J. M. 1995. The 1852 and 1868 Mauna Loa picrite eruptions; clues to parental magma compositions and the magmatic plumbing system. *Geophysical Monograph* 92:241–262.

Rowland S. K., Harris A. J. L., and Garbeil H. 2004. Effects of Martian conditions on numerically modeled, cooling-limited, channelized lava flows. *Journal of Geophysical Research (Planets)* 109, doi: 10.1029/2004JE002288.

Rutherford M. J., Calvin C., Nicholis M. G., and McCanta M. C. 2005. Petrology and melt compositions in nakhlite MIL 03346: Significance of data from natural sample and from experimentally fused groundmass and M.I.'s (abstract #2233). 36th Lunar and Planetary Science Conference. CD-ROM.

Rutherford M. J. and Hammer J. E. 2008. Oxidation states in MIL 03346 nakhlite from experiments reproducing phenocryst-melt equilibria as a function of fO_2 and T at 40–150 MPa (abstract #1983). 39th Lunar and Planetary Science Conference. CD-ROM.

Saar M. O., Fremouw S., Manga M., and Cashman K. V. 2001. Numerical models of the onset of yield strength in crystal-melt suspensions. *Earth and Planetary Science Letters* 187:367–379.

Sato H. 1995. Textural difference between pahoehoe and a'a lavas of Izu-Oshima Volcano, Japan—An experimental study on population density of plagioclase. *Journal of Volcanology and Geothermal Research* 66:101–113.

Self S., Keszthelyi L., and Thordarson T. 1998. The importance of pahoehoe. *Annual Review of Earth and Planetary Sciences* 26: 81–110.

Shaw H. 1972. Viscosities of magmatic silicate liquids: An empirical method of prediction. *American Journal of Science* 272:870–889.

Thordarson T. and Self S. 1993. The Laki (Skaftar-Fires) and Grimsvotn eruptions in 1783–1785. *Bulletin of Volcanology* 55: 233–263.

Treiman A. and Goodrich C. A. 2001. A parent magma for the Nakhla martian meteorite: Reconciliation of estimates from 1-bar experiments, magmatic inclusions in olivine, and magmatic inclusions in augite (abstract #1107). 32nd Lunar and Planetary Science Conference. CD-ROM.

Treiman A. H. 1993. The parent magma of the Nakhla (SNC) meteorite, inferred from magmatic inclusions. *Geochimica et Cosmochimica Acta* 57:4753–4767.

Treiman A. H. 2005. The nakhlite meteorites: Augite-rich igneous rocks from Mars. *Chemie der Erde-Geochemistry* 65:203–270.

Turcotte D. L. and Schubert G. 1982. *Geodynamics: Applications of continuum physics to geological problems*. New York: John Wiley & Sons. 449 p.

Underwood E. E. 1968. Surface area and length in volume. In *Quantitative microscopy*, edited by DeHoff R. T. and Rhines F. N. New York: McGraw-Hill. pp. 78–127.

Wagner T. P., Donnellynolan J. M., and Grove T. L. 1995. Evidence of hydrous differentiation and crystal accumulation in the low-MgO, high-Al_2O_3 lake basalt from Medicine Lake volcano, California. *Contributions to Mineralogy and Petrology* 121:201–216.

Walker D., Kirkpatrick R. J., Longhi J., and Hays J. F. 1976. Crystallization history of lunar picritic basalt sample 12002; phase-equilibria and cooling-rate studies. *Geological Society of America Bulletin* 87:646–656.

Wyllie P. J., Donaldson C. H., Irving A. J., Kesson S. E., Merrill R. B., Presnall D. C., Stolper E. M., Usselman T. M., and Walker D. 1981. *Experimental petrology of basalts and their source rocks*. New York: Pergamon Press.